Article

Development of a Flow Rule Based on a Unified Plasticity Model for 13Cr-4Ni Low-Carbon Martensitic Stainless Steel Subject to Post-Weld Heat Treatment

Mir Mehrdad Hosseini [1], Jacques Lanteigne [2], Carlo Baillargeon [2], Mohammad Jahazi [1] and Henri Champliaud [1,*]

[1] Department of Mechanical Engineering, École de Technologie Supérieure, 1100, Notre-Dame Street West, Montreal, QC H3C 1K3, Canada; mohammad.jahazi@etsmtl.ca (M.J.)

[2] Institut de Recherche d'Hydro-Québec (IREQ), 1800, Boul. Lionel-Boulet, Varennes, QC J3X 1S1, Canada

* Correspondence: henri.champliaud@etsmtl.ca

Abstract: This study aims to develop a flow rule for evaluating the relaxation and redistribution of residual stresses during the post-weld heat treatment (PWHT) of hydroelectric runners made from low-carbon martensitic stainless steel (13Cr-4Ni composition). During the PWHT, austenite reforms in the filler metal and surrounding areas of the base metal near welded joints. The evolving inelastic strain rate with reformed austenite led to defining two distinct flow rules in the pure martensitic (α') and austenitic (γ) phases. A linear rule of mixture was then applied to assess global effective stress based on the inelastic strain rate and current austenite fraction during the PWHT. A unified constitutive model incorporating drag stress and back stress, evolving with creep and plastic deformation mechanisms during the PWHT, described the stress–strain behavior. To validate this analysis, a third flow rule was determined in the 18% tempered austenitic microstructure, compared with the rule of mixture's effective stress contribution from each phase on the inelastic strain rate. Isothermal constant strain rate tests in stabilized crystalline microstructures evaluated constants specific to their respective flow rules. This study demonstrates the stability of reformed austenite at elevated temperatures during slow cooling and its significant influence on the mechanical properties of 13Cr-4Ni steels. The effectiveness of estimating yield stress using the rule of mixture based on individual phase behaviors is also confirmed.

Keywords: martensitic stainless steels; tempering; flow rule; strain rate

1. Introduction

Large hydraulic turbine runners are currently manufactured from low-carbon martensitic cast stainless steel of grade CA6NM with a composition of 13Cr-4Ni. The blades are assembled by homogeneous multipass welding to the crown and band of the runner using the flux-cored arc welding (FCAW) process using the filler metal E410NiMo of the same composition.

This welding assembly is a complex process, and it can last several months. At the end of the welding process, a post-weld heat treatment (PWHT) is applied to the entire runner.

Upon completion of the welded assembly and before the PWHT, the filler metal is 100% martensitic on the surface and may contain a small amount of reformed austenite at the root of the weld joints due to the deposition of successive layers of filler metal. The CA6NM base metal may also contain a small amount of reformed austenite in the regions surrounding the weld joints and within the heat-affected zone (HAZ).

Moreover, as shown in the next section, further from the weld, the base metal remains between 15% and 20% austenite content throughout the manufacturing process, with the remainder being tempered martensite. This stabilized austenite microstructure of the cast steel is obtained from tempering at 620 °C at the supplier's foundry. The tempering heat

treatment restores good mechanical properties and ensures good weldability. It is worth noting that 13Cr-4Ni steel is not suitable for serving in as-cast or as-welded conditions due to its poor ductility and fracture toughness, as it contains only untempered martensite.

Residual stresses (RSs), which can have a profoundly negative impact on component quality and performance, reach their maximum level at the end of the weld assembly. At this point, a 2 h tempering at 620 °C followed by a slow cooling is applied to maintain the entire reformed austenite in a stable state during the plateau, whereby the RS level ultimately falls to an acceptable level of below 50 MPa in the welded joints. However, there are situations in which the residual stress remains much higher, which may lead to the initiation of fatigue cracks during the startup of turbine–generator units. It is therefore essential to know the initial state of RSs and their evolution during the PWHT.

To describe the evolution of stresses during the PWHT, we propose to develop a flow rule that would be a function of the austenite content (γ) during the PWHT. To this end, a linear rule of phase mixture is proposed. This requires the development of three distinct flow rules, one for each stabilized pure microstructure, namely:

The fully martensitic condition with 100% α', which corresponds to the initial state at the start of the PWHT;

The fully austenitic condition with 100% γ;

The fully tempered condition with 18% γ, which corresponds to the final state at the end of the PWHT, to validate the rule of mixture.

The rule of mixture consists in adding the yield stress of the martensitic phase (1) weighted by the volume fraction of martensite to the yield stress of the austenitic phase (2) weighted by the volume fraction of austenite. Thus, the initial mixture at the start of the PWHT consisting of 100% α'–0% γ becomes 82% α'–18% γ at the end. This reconstruction of the flow rule should agree, in the final state, with the flow rule (3) obtained independently of the other two.

Viscoplastic models are widely utilized in research, as extensively discussed in Krempl's review paper [1], which serves as a comprehensive resource on the subject. However, microstructural changes due to phase transformation are not addressed in his paper.

Post-heat treatments, often necessary in welded assemblies, are also crucial for additive-manufactured products, where they aim to relieve residual stress and enhance mechanical performance. For instance, Li et al. optimized the microstructure of Inconel alloy 718, significantly improving its tensile properties [2]. Despite these advancements, no model has been proposed to comprehensively predict material response under thermal loading. Efforts have focused on unified constitutive modeling to understand material behavior under thermomechanical coupling, as demonstrated by Lei et al.'s unified model [3]. However, empirical validation of such models remains necessary.

The present study addresses the development of the flow rule of a 13Cr-4Ni low-carbon martensitic stainless steel subject to post-weld heat treatment. The constants of the model were determined from prescribed isothermal strain rate tests.

To assess the inelastic strain rate, the unified plasticity approach of Engler-Pinto et al. [4], adapted from the original approach developed by Sehitoglu [5] and Slavik and Sehitoglu [6], was used. This is a flow rule in which the stresses evolve over time in accordance with the creep or plastic deformation mechanisms that are activated during the PWHT. Similar approaches were proposed by Li et al. [7] and Hosseini et al. [8].

These two state variables depend essentially on the effective stress, the temperature, and the time of exposure to elevated temperatures. This dependence is expressed by two functions evolving over time according to the strain history. To integrate the inelastic strain rate over time, the two evolving functions must therefore be known beforehand. They include constants that must be determined by targeted tests. These developments are the subject of a second study currently underway.
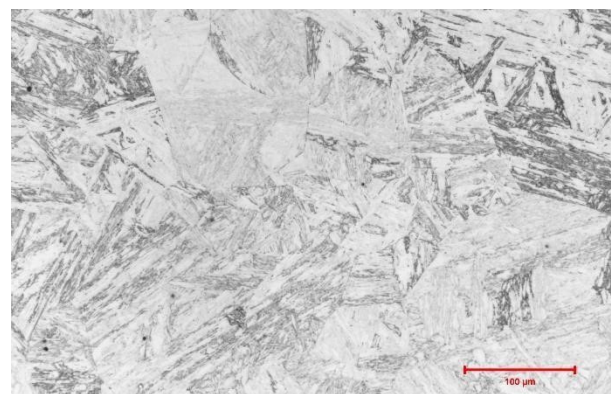
2. Microstructure

2.1. Microstructural Changes Occurring during the PWHT

During tempering at 620 °C from the as-quenched martensitic state or the as-welded state, which is equivalent in terms of microstructure, significant changes occur in the substructure of the steel. From 500 °C up to 620 °C, the hardness drops, and the residual stresses gradually fade away [9]. The microstructure then consists of primary austenite grains (PAGs), which are formed at high temperatures when the steel is cast. Martensite laths then form within the PAGs upon quenching in air. That can be observed in Figure 1. It is only at 550 °C that austenite begins to form between the martensite laths. These laths can only be resolved at a nanometric scale [10]. Indeed, in Figure 1, using conventional optical metallography, there are no apparent differences observed for the as-quenched and tempered states. It should be noted that the differences cannot be observable at this scale.
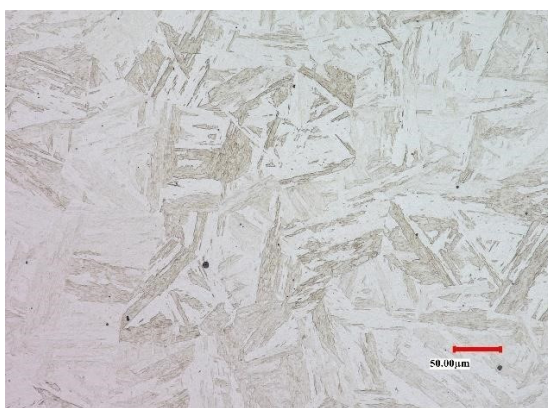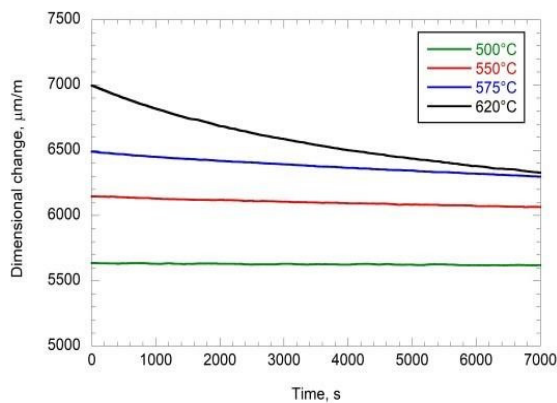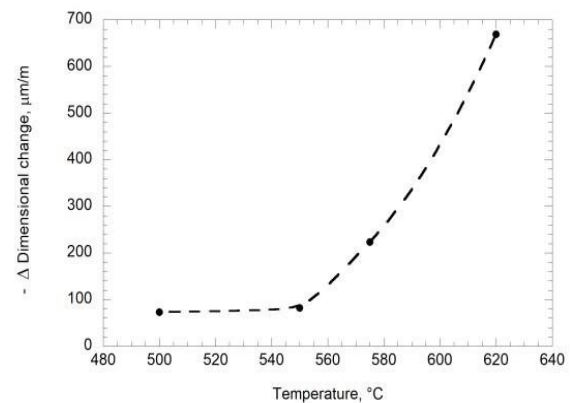

(**a**) As-quenched

(**b**) Quenched and tempered

Figure 1. SS415 microstructure. From optical metallography, the same features are observed, with the only apparent difference being the relatively higher sensitivity to the etching in the Q and T state.

Figure 2 shows the evolution of the dimensional changes taking place during stays at 500 °C, 550 °C, 575 °C, and 620 °C. As it can be seen, the shrinkage of the crystal lattice is barely noticeable at 550 °C when compared to 620 °C, where the austenitic transformation prevails. Nevertheless, the tetragonality of the martensitic phase during the stay at 550 °C gradually approaches the BCC crystal structure of iron, and complex carbides of chromium and molybdenum are formed [11]. This results in a substantial gain in ductility and fracture toughness [12].

(**a**)

(**b**)

Figure 2. (**a**) Dilatometric test results from the as-quenched condition for selected temperatures; (**b**) dimensional change that occurred after a 2 h stay at each temperature.

2.2. Reformed Austenite Measurements in Tempered 13Cr-4Ni Steels

The measurement of austenite in 13Cr-4Ni steels is generally carried out using the X-ray diffraction (XRD) method following the protocol of the ASTM E975 standard [13] or employing the Rietveld refinement method [14,15]. It is now generally accepted that the maximum content is obtained by tempering for 2 h at 620 °C from the as-quenched condition [15–17].

Côté [18] compared various measurement techniques on samples taken from a SS415 wrought steel plate austenitized and tempered for 2 h at 620 °C. This steel has the same chemical composition as the CA6NM cast steel. XRD measurements gave an austenite content of 15.3%. Measurements obtained by Electron Backscatter Diffraction (EBSD) gave contents between 15% and 20%, whereas measurements obtained by dilatometry gave a maximum content of 18.4%. On the same steel grade and in the as-received condition (i.e., duly tempered), Fréchette [9] measured a content of 18.2% using XRD.

Moreover, other researchers have reported much lower XRD measurements for steels of the same composition and identical thermal history. For example, Robichaud [19] obtained 10%, and Chaix [20] obtained 6%.

This large variability in the XRD measurements can be explained, at least in part, by the influence of the cooling rate. Fréchette [9] compared the value of 18.2% for the SS415 steel he obtained after a controlled cooling in the oven to that of 12.6% he obtained after cooling from 620 °C in water. As part of the present study, we repeated this same experiment of quickly removing small samples from the oven after a stay of 2 h at 620 °C from the as-quenched state. The XRD Rietveld refinement method was applied using TOPAS 3.9 software with scans obtained in rotation, as greater accuracy is obtained when scanning is performed while the sample is rotating, although XRD measurements can be obtained using a line scan. And, in stark contrast to the expected value of 18%, values varying between 8.1% and 9.6% were obtained. The dilatometric curves shed some light on the issue. When the cooling rate increases after tempering, a martensitic transformation is observed on the dilatometric curve, which explains why a significant fraction of the austenite reformed at 620 °C may then become unstable and transform back into martensite. However, no transformation is observed at a low cooling rate. This is illustrated in Figure 3.
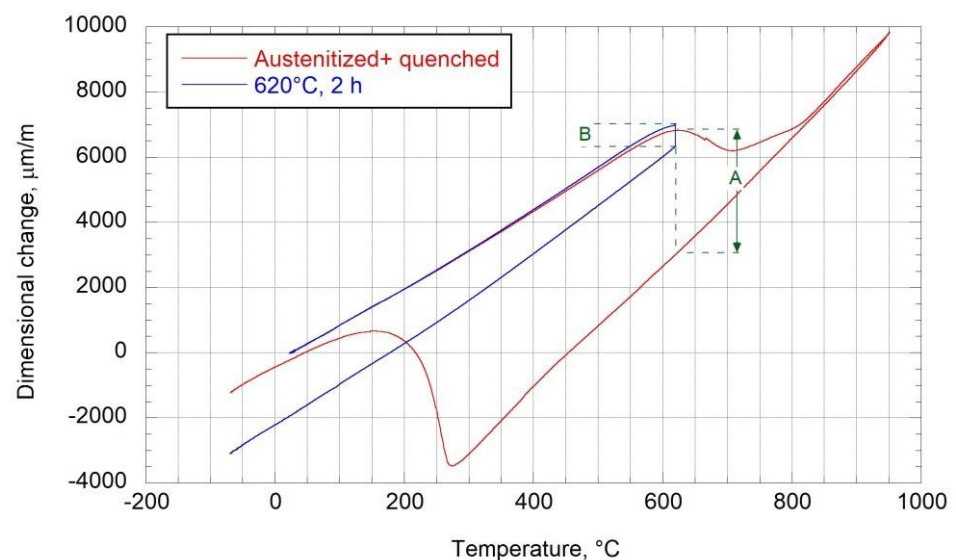
Figure 3. Specimen 1 (red curve): complete thermal cycle from the fully martensitic (as-quenched) condition; specimen 2 (blue curve): tempering for 2 h at 620 °C from the fully martensitic state.

Starting from the fully martensitic as-quenched condition, two samples are heated at a rate of 1 °C/min and cooled at the same rate. The austenitic transformation begins around 620 °C. The first sample (red curve) is heated up to 950 °C, where the steel becomes entirely

austenitic and remains so upon cooling down to 270 °C, at which point the martensitic transformation starts. The second sample (blue curve) is maintained for 2 h at 620 °C, then cooled down to −70 °C. In this case, no martensitic transformation is observed.

Segment A in Figure 3 corresponds to the dimensional change with 100% austenite at 620 °C, while segment B represents the dimensional change due to reformed austenite during tempering at the same temperature. The ratio B/A obtained is 0.188, which represents 18.8% austenite reformed at 620 °C, which in this case remained stable upon cooling.

Besides the cooling rate, the maximum temperature reached is another equally important factor. Figure 4 shows that at 625 °C and above, the austenite becomes progressively unstable and transforms back into martensite upon cooling at any rate.
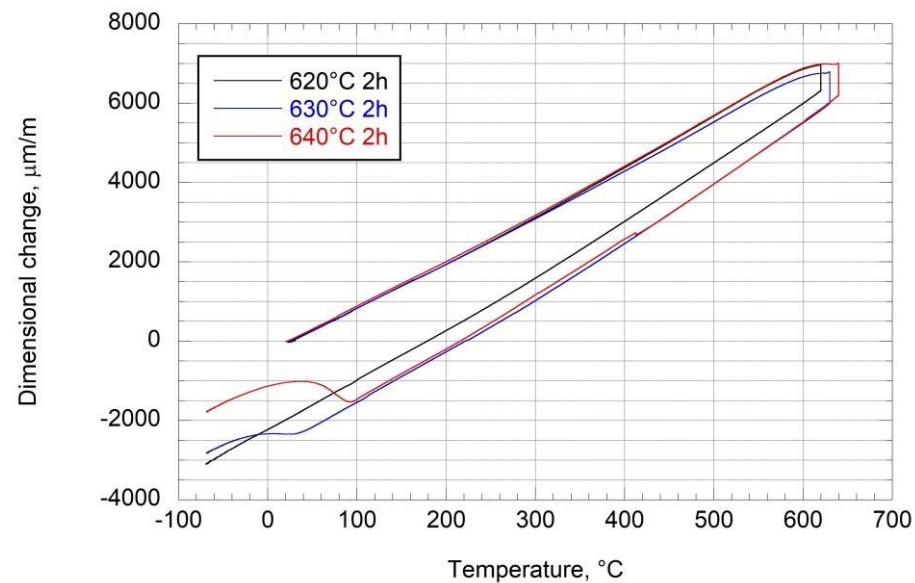

Figure 4. Martensitic transformation occurs upon cooling at temperatures above 625 °C, even at low cooling rates.

However, turbine runner manufacturers have long held the maximum tempering temperature at 620 °C, while the minimum is set at 600 °C, and the maximum prescribed cooling rate is −25 °C/h. This explains the value of 18% obtained in as-received duly tempered plates from suppliers.

3. The Basis of the Constitutive Relation within the Unified Model

3.1. The Additivity of Strain Components

It is generally accepted that the total deformation can be expressed by the addition of its different components. At any point in a thermomechanical process, we may then say the following:

$$\dot{\epsilon} = \dot{\epsilon}^{mech} + \dot{\epsilon}^{tr} + \dot{\epsilon}^{th} \tag{1}$$

where the total strain rate is the summation of the strain rate due to the applied loads plus the strain rates due to the phase transformation plus the free thermal strain (FTS).

In the specific case of the dilatometric test in a virgin sample (as in Figures 2–4), when no load is applied, the total strain rate is simply due to the phase transformation and the FTS. Equation (1) then reduces to the following:

$$\dot{\epsilon} = \dot{\epsilon}^{tr} + \dot{\epsilon}^{th} \tag{2}$$

Within the temperature range of interest for this study, i.e., 20 °C to 620 °C, the tempering of martensite has negligible effect on $\dot{\epsilon}^{tr}$, as discussed previously (see Figure 2). Therefore, $\dot{\epsilon}^{tr}$ comes almost exclusively from the γ-phase (reformed austenite) transformation.

The mechanical strain rate can also be divided into two components, the elastic strain rate and the inelastic strain rate, with the former being simply the stress rate divided by the Young's modulus.

$$\dot{\epsilon}^{mech} = \dot{\epsilon}^{e} + \dot{\epsilon}^{in} = \frac{\dot{\sigma}}{E} + \dot{\epsilon}^{in} \tag{3}$$

As presented in the next section, the inelastic strain component represents either viscoplasticity (i.e., creep strain) or time-independent plasticity (i.e., rate-insensitive plasticity).

The stress and strain components in Equations (1)–(3) are all tensor entities that depend on time and temperature. Subscripts are omitted here to simplify the presentation. For example, the thermal strain rate $\dot{\epsilon}^{th}$ is given as $\alpha T \delta_{ij}$, where α is the coefficient of thermal expansion, which depends on temperature; T is the temperature rate, and δ_{ij} is the Kronecker delta.

3.2. The Rule of Mixture in a Two-Phase Homogeneous Microstructure

Since the early 1980s, the scientific community has rejected the hypothesis of the additivity of deformation in a multi-phase mixture. As Leblond [21] commented, experimental evidence shows that if a deformation is imposed on a two-phase polycrystalline structure, the two phases are then subject to the same macroscopic deformation. There will be incompatibility deformations at the microscopic scale that will cause internal stresses, but overall, it is conceivable that the stress during the plastic flow of the mixture will be a global yield given by the average of the stress on each phase weighted by their relative proportion in the mixture.

However, Leblond [21] asserts that the application of such a simple rule of phases by other researchers is by itself representative of an oversimplified view of more complex behavior at a microscopic scale. He then adds that it is difficult for any researcher to demonstrate experimentally the validity of the assumption of the application of the rule of phase mixture since the literature does not provide any example where it is possible to measure the properties of each phase individually and maintain their stable proportion during an isothermal deformation, as in most cases, loading results in a phase transformation.

In the present study, however, we manage to maintain the two phases individually stable during isothermal deformation, as we will see in Section 3. We will therefore verify the assumption that the yield stress of a mixture can be estimated from that of its constituents, as described below:

During the PWHT of 13Cr-4Ni steel, the relative proportion of the two phases present, α' and γ, varies. We thus assume that a linear rule of mixture can be used to differentiate the contribution of each phase to the global yield of the mixture. As discussed previously, the austenitic phase is homogeneously distributed within the martensite laths at the nanoscale. This assumption thus seems appropriate. The rule can be expressed as follows:

$$\sigma_y^{mix} = f_\gamma \, \sigma_y^\gamma + (1 - f_\gamma) \, \sigma_y^{\alpha'} \tag{4}$$

where f_γ is the volume fraction of reformed austenite, σ_y^{mix} is the global yield, σ_y^γ is the yield of the austenite phase, and $\sigma_y^{\alpha'}$ is the yield of the martensitic phase.

3.3. The Unified Flow Rule

Engler-Pinto et al. [19] proposed a unified model that has proven effective in describing creep and plasticity at elevated temperatures in aluminum alloys subjected to thermomechanical stress cycles. It was adapted from a model originally developed by Sehitoglu [21] and Slavik et al. [20] for low-alloy carbon steels. This flow rule seemed suitable to describe the viscoplastic flow in 13Cr-4Ni steels subjected to elevated temperatures and with an initially high level of residual stresses. It is expressed as follows:

$$\dot{\epsilon}_{ij}^{in} = \frac{3}{2} A(T) \, f\left(\frac{\overline{\sigma}}{K}\right) \frac{S_{ij} - S_{ij}^c}{\overline{\sigma}} \tag{5}$$

where $A(T)$ is a function of temperature, $\overline{\sigma}$ is the effective stress, K is the drag stress, $f(\overline{\sigma}/K)$ is a scalar function that depends on the ratio $\overline{\sigma}/K$, S_{ij} is the deviatoric stress tensor, and S_{ij}^c is the deviatoric back-stress tensor. Effective stress is defined as follows:

$$\overline{\sigma} = \sqrt{\frac{3}{2}\left(S_{ij} - S_{ij}^C\right)\left(S_{ij} - S_{ij}^C\right)} \tag{6}$$

Substituting Equation (6) in Equation (5), noting that the effective strain rate is defined as $\dot{\epsilon} = \sqrt{\frac{2}{3}\dot{\epsilon}_{ij}^{in}\dot{\epsilon}_{ij}^{in}}$, it becomes

$$\dot{\overline{\epsilon}}^{in} = A(T)f(\overline{\sigma}/K), \tag{7}$$

with $A(T)$ given as

$$A(T) = A_c \, e^{-Q/R(T+273)}, \tag{8}$$

where A_c is a material constant, Q is the thermal activation energy for creep, R is the universal gas constant, and T is the temperature in degrees Celsius. A_c and Q are to be determined from experiments. The term 273 comes from converting the temperature from degrees Celsius to Kelvin, since an Arrhenius-type relationship is always expressed in Kelvin.

In this unified theory, the creep and plastic strains are merged as a total inelastic strain, and the yield surface is replaced by a stress surface, as shown in Figure 5. The traditional concept of a yield surface in plasticity defines a distinct boundary between elastic and plastic deformation based on the material's yield stress. In the context of the unified theory, the substitution of the yield surface with a stress surface suggests the creation of a broader boundary that encompasses both elastic and viscoplastic states of stress in a more comprehensive manner. This model is governed by two state variables, the "drag stress" and the "back stress", which describe the extent and location of the stress surface. In the deviatoric stress space, these variables stand for the growth (scalar value) of the stress circle and the position (tensorial value) of its center, respectively. Physically, these terms have micro-feature definitions. The drag stress depends on dislocation density and their arrangements, which represent the number of blocked dislocations, whereas the directional stockup of dislocations at precipitates and other potential obstacles like boundaries stand for the back stress.
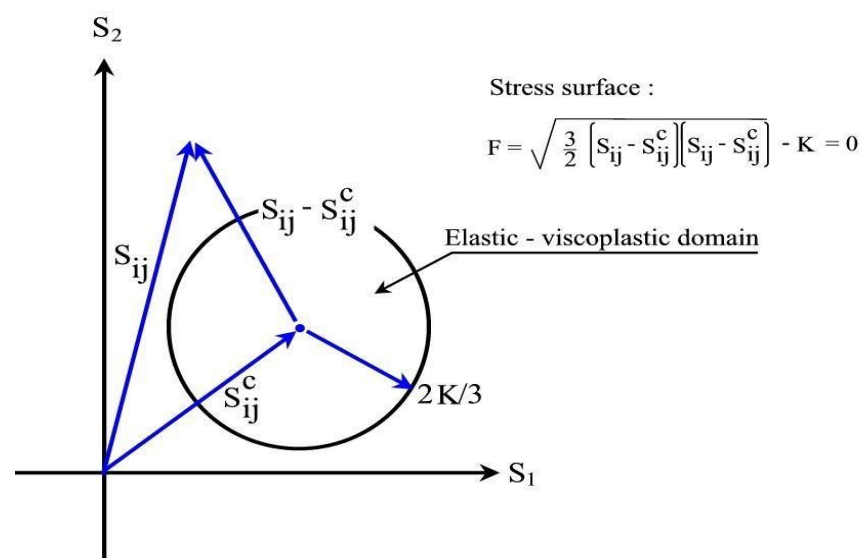

Figure 5. Representation of the stress surface in the deviatoric stress space.

Thus, depending on the ratio $\overline{\sigma}/K$, the scalar function f in Equation (5) may exhibit two different behaviors. For a stress state located inside the stress surface, i.e., $\overline{\sigma}/K < 1$,

the steel shows sensitivity to the rate of deformation typical of creep, while outside the stress surface, i.e., $\overline{\sigma}/K \geq 1$, where the strain rate is higher, it becomes time-independent and plasticity deformation mechanisms prevail.

The following scalar functions are suggested:

$$
f\left(\frac{\overline{\sigma}}{K}\right) = \begin{cases} \left(\frac{\overline{\sigma}}{K}\right)^{n_1}, & \frac{\overline{\sigma}}{K} < 1 \\ e^{\left[\left(\frac{\overline{\sigma}}{K}\right)^{n_2} - 1\right]}, & \frac{\overline{\sigma}}{K} \geq 1 \end{cases} \tag{9}
$$

where n_1 and n_2 are two material constants to be determined from experiments. Preliminary tests carried out under sustained loads representative of RS measured on site at elevated temperatures (such as during the PWHT) confirmed that creep deformation was significant. Therefore, this formulation of the stress–strain constitutive relation seemed appropriate to describe stress relaxation for this material in similar conditions.

The integration of the flow rule over time depends on how the two governing state variables and the effective stress evolve with temperature.

The drag stress K depends on the temperature and the effective stress, which, at a given inelastic strain rate, is affected by the isotropic hardening factor. Furthermore, a recovery factor depending on the time of exposure to elevated temperatures may also influence the drag stress.

Moreover, the internal stress (i.e., the deviatoric back stress S_{ij}^c) also varies as a function of the inelastic strain rate due to the kinematic hardening factor and a possible dynamic recovery factor.

Except for the dependence of drag stress on temperature, which is estimated in this article, all other dependencies of the two state variables are expressed by functions comprising constants that should be determined by experiments. This is the subject of a separate, ongoing study.

This article mainly focuses on the determination of the constants in Equations (7)–(9), allowing the development of the flow rule as a function of the austenite volume fraction.

4. Equipment and Specimen Preparation

4.1. Equipment

Figure 6 illustrates a furnace entirely designed to perform isothermal constant strain rate tests to determine the yield stress in compression in different metallurgical conditions, namely in the as-quenched, tempered, and fully austenitized conditions. It can reach 1000 °C and maintain the setpoint stably over several days to an accuracy of one degree. It is mounted on an Instron 4488 electromechanical test bench with a capacity of 100 kN, equipped with the Bluehill Universal interface testing software from the same manufacturer. The minimum prescribed crosshead displacement rate is 10^{-8} mm/s.

A 100 kN Instron 8002 servo-hydraulic test frame with an 8800 console interface from the same manufacturer was used to measure the Young's modulus in tension in the three microstructures at various temperatures. It is equipped with a high-temperature extensometer and a 15 kW Lepel induction heating system. Constant displacement rate tests were also conducted to measure the yield stress in tension in this testing facility, which were compared to similar data previously obtained in compression. The minimum allowed displacement rate on this system is 1.67×10^{-5} mm/s.
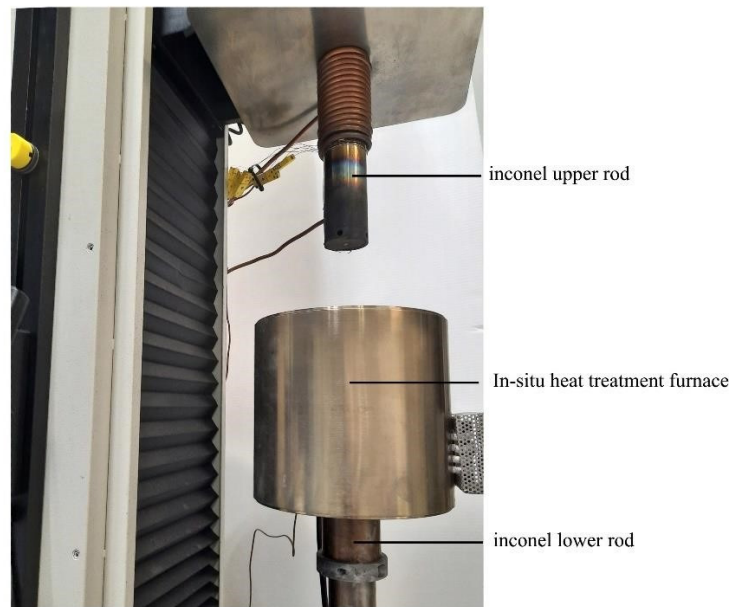
Figure 6. Furnace designed for testing in situ heat-treated specimens at constant stain rates.

4.2. Material and Specimen Preparation

As part of this study, SS415 wrought steel with the same composition and microstructure as CA6NM and E410NiMo was used for the experimental program. Its composition is shown in Table 1. This steel does not contain large casting or weld defects, such as those found in cast steels and filler metals. It is therefore more suitable for reducing as much scattering as possible in the data.

Table 1. S41500 (Wt%).

C	Mn	S	P	Si	Ni	Cr	Mo
0.014	0.80	0.001	0.014	0.46	4.45	12.06	0.63

As mentioned in the introduction, it is not possible to differentiate during tests the sole contribution of the reformed phase γ from that of phase α' on the strain rate during the PWHT, nor is it possible to perform an experiment at a prescribed strain rate when a phase transformation is ongoing. Dimensional stability is necessary.

However, stable microstructures with either 0%, 18%, or 100% austenite can be achieved from in situ heat treatment in the testing facilities. This allows, using a rule of mixture, to reconstruct the properties of a mixture with varying levels of austenite and to isolate the contribution of each phase all along a PWHT.

There are, however, limitations on the temperature range for which the material is stable during isothermal tests. After an austenitizing treatment, the austenite is stable at $f_\gamma = 1$ from M_s, the martensitic phase transformation start temperature, which is approximately 280 °C, to 620 °C. After a tempering heat treatment, the reformed austenite is stable at $f_\gamma = 0.18$ from ambient to 620 °C. Finally, in the as-quenched condition, $f_\gamma = 0$, the fully martensitic microstructure is stable from ambient to 550 °C. The dilatometric curves in Figure 7a illustrate the thermal paths followed to condition these microstructures.

The SS415 steel plate was austenitized for 1 h at 1050 °C and naturally quenched in air. The samples were therefore all initially in the as-quenched condition. For the isothermal compressive tests, the specimens are cylinders of 5 mm in diameter and 10 mm in length. Their longitudinal axis is aligned in the direction of the rolling of the plate. Before starting the test, the specimen is heated to the temperature assigned for the test, then loaded at the prescribed nominal total displacement rate. Strain rates are calculated by subtracting

the machine displacement due to load frame compliance from the total displacement and normalizing this displacement relative to the initial specimen length.
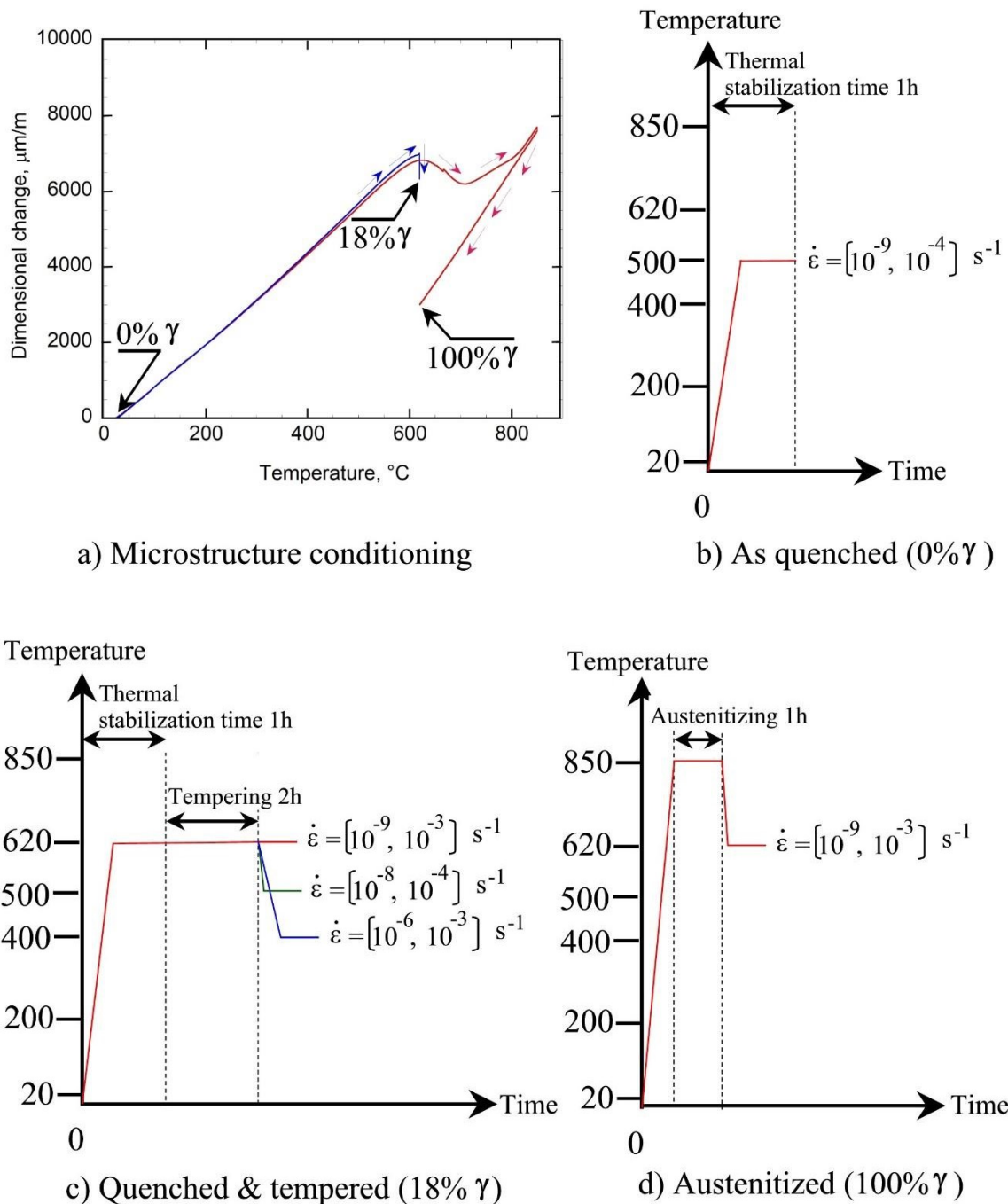

a) Microstructure conditioning

b) As quenched (0%γ)

c) Quenched & tempered (18% γ)

d) Austenitized (100%γ)

Figure 7. Diagram illustrating (**a**) in-situ heat treatments performed to get different stable microstructures, in blue: heating up to 620 °C maintain 2 h, in red: heating up to 850 °C, maintain 1 h, cool down to 620 °C; (**b**–**d**) ranges of prescribed strain rates.

Constant strain rate tests in tension and Young's modulus measurements were also conducted on the servo-hydraulic test facility equipped with a Lepel induction heater and a high-temperature extensometer. Specimens with diameters of 3/8 in and gauge lengths of 2.25 in were employed.

Creep tests were carried out on both test facilities (i.e., in tension and compression) to determine the thermal activation energy for creep.

5. Determination of the Constants for the Model

5.1. Determination of the Thermal Activation Energy for Creep

The thermal activation energy Q in Equation (8) was estimated from creep tests. In the secondary creep stage, the creep rate is linear, and, at constant applied stress, the creep rate is given as in [22]:

$$\dot{\epsilon}^{cr}(\sigma, T) = k(\sigma)\, e^{-Q/R(T+273)} \tag{10}$$

where $\dot{\epsilon}^{cr}(\sigma, T)$ is the creep rate at constant stress σ, k is an unknown function of stress, T is the temperature in Celsius, and R, the universal gas constant, is 8.314 J/mol-K. Two tests at equal stress were performed at T_1 and T_2, with $T_2 > T_1$. From Equation (10), we have the following:

$$Q = R \frac{ln\left(\frac{\dot{\epsilon}^{cr}(\sigma, T_2)}{\dot{\epsilon}^{cr}(\sigma, T_1)}\right)}{\left[\frac{1}{T_1} - \frac{1}{T_2}\right]} \tag{11}$$
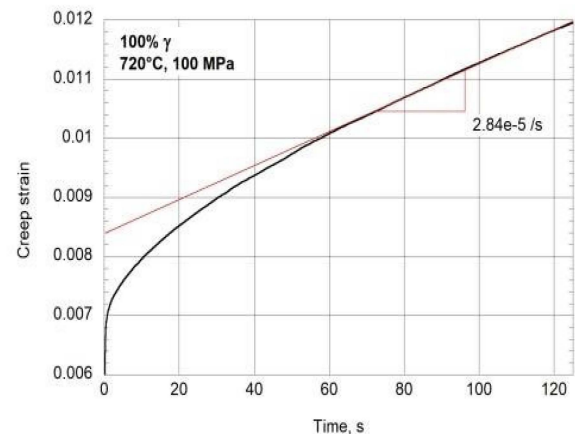
Table 2 presents the results obtained for the three microstructures under study. Figure 8 illustrates the test results for $f_\gamma = 1$.

Table 2. Creep test results.

Austenite Fraction, f_γ	Q (J/mol)	Stress (MPa)	T_1 (°C)	T_2 (°C)	$\dot{\epsilon}^{cr}(\sigma, T_1)$ (s^{-1})	$\dot{\epsilon}^{cr}(\sigma, T_2)$ (s^{-1})
0	3.27×10^5	325	500	550	1.04×10^{-8}	2.29×10^{-7}
0.18	3.28×10^5	325	550	620	2.80×10^{-7}	1.13×10^{-5}
1.0	3.45×10^5	100	620	720	2.63×10^{-7}	2.84×10^{-5}
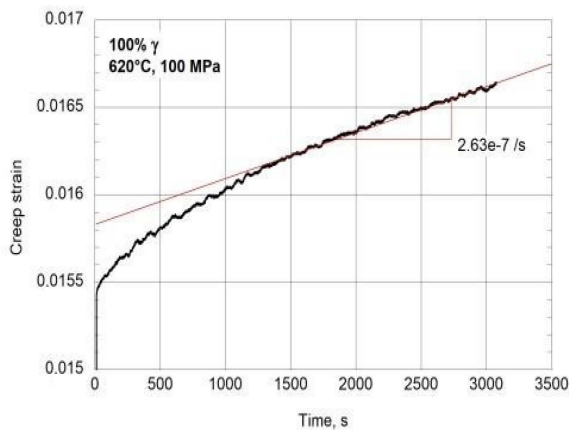
(**a**) At 620 °C

(**b**) At 720 °C

Figure 8. Creep tests carried out in pure austenite.

5.2. Determination of the Yield Stress

The yield stress σ_y was determined from isothermal constant strain rate tests in compression at the very onset of plasticity, i.e., at the point of departure from linearity of the initial stress–strain curve. Figure 9a illustrates an example where the yield stress was estimated at 510 MPa. In all tests, the strain at the point of departure from linearity was estimated within 5×10^{-5}.
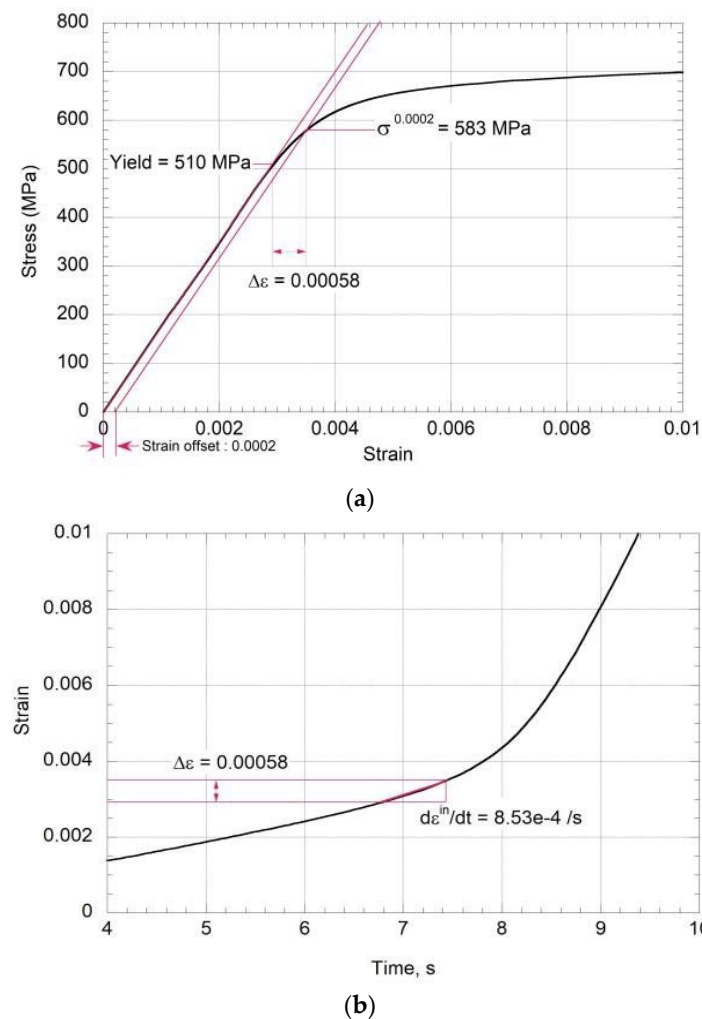
(a)

(b)

Figure 9. Stress–strain curve obtained at 400 °C at a nominal strain rate of 1×10^{-2}/s. (**a**) Estimation of yield at the onset of plasticity and at 2×10^{-4} inelastic strain offset. (**b**) Estimation of the inelastic strain rate at the onset of plasticity.

The strain rate at this point was estimated at a small plastic strain offset of 2.0×10^{-4}, as shown in Figure 9a. The yield at this strain offset was estimated at 583 MPa in this example. The strain rate in the interval from the actual strain at yield to that at an offset of 2×10^{-4} is estimated at 8.53×10^{-4} /s. This is illustrated in Figure 9b.

As this figure shows, the measured strain rate at the onset of plasticity is lower than the prescribed nominal rate, which is 1.0×10^{-2} /s in this example. This is an undesirable effect of a low-rigidity frame. As mentioned previously, the stress–strain curve is derived from a calculation in which the machine displacement due to frame compliance has been subtracted from the total displacement. However, as it is the total displacement rate that controls the test, some fraction of this displacement is due to the frame displacement, and this fraction depends on the relative rigidity of the sample as compared to that of the test frame.

The relative rigidity of the frame compared to the sample is higher in the plastic domain than in the elastic domain. Consequently, when the plasticity is fully developed, the sample strain rate approaches the nominal rate. This does not affect the stress–strain curve but results in a continuous change in rate as the test progresses. Since the objective is to capture the strain rate at the onset of viscoplasticity, we estimate that the value measured with an offset of 2×10^{-4}, as illustrated in Figure 9, represents the exact rate in the targeted area.
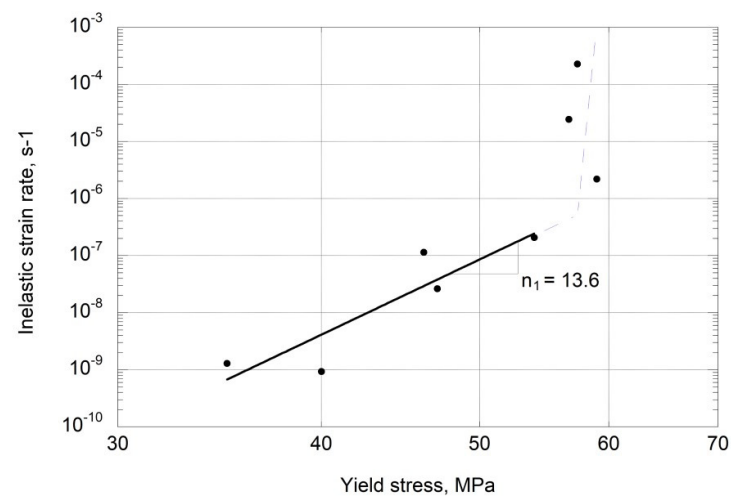
Following the procedure described above, tests were carried out in accordance with the parameters specified in Figure 7b–d. The results are presented in Figure 10a–c.

(**a**) 0% γ at 500 °C
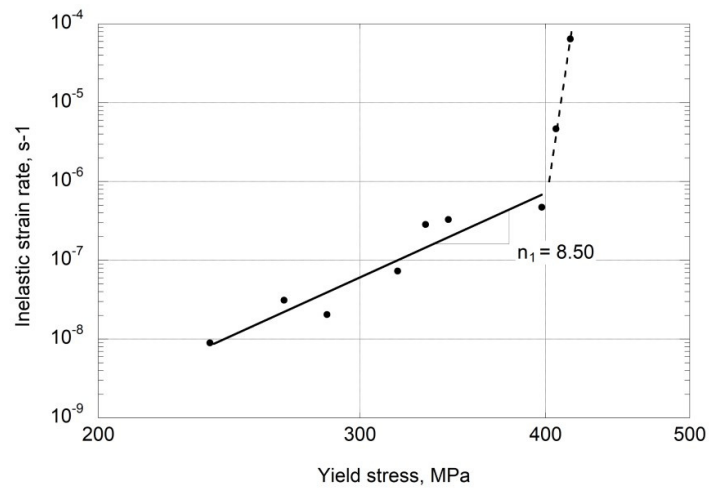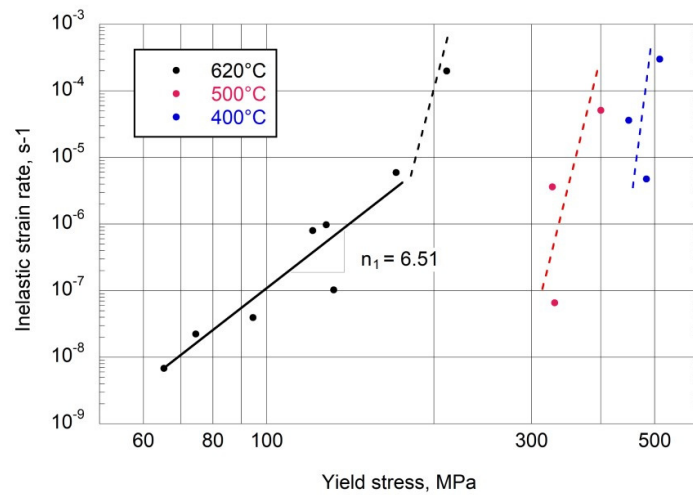
(**b**) 18% γ at 620 °C, 500 °C, and 400 °C

(**c**) 100% γ at 620°C

Figure 10. The influence of the strain rate on the yield stress.

For the same temperature and a given microstructure, two regimes of inelastic deformation can be observed, the first showing sensitivity to the deformation rate (in solid lines) and the second (in dashed lines) a mode of deformation for which the elastic limit depends much less on the deformation rate.

Initially, the samples are virgin, so the back stress is zero, while the initial drag stress is designated K_0 as the reference at the temperature of the test. In the first regime, i.e., in the viscoplastic flow (solid lines in Figure 10), based on Equation (7) of the model and the appropriate scalar function in Equation (9) for this regime, i.e., $\overline{\sigma}/K_0 < 1$, we have $\overline{\sigma} = \sigma_y$:

$$\left(\frac{\dot{\overline{\epsilon}}^{in}}{A} \right) = \left(\frac{\sigma_y}{K_0} \right)^{n_1} \tag{12}$$

That is,

$$ln\ \dot{\overline{\epsilon}}^{in} = ln\ A + n_1\ ln\ \sigma_y - n_1\ ln\ K_0 \tag{13}$$

As an example, the best linear fit of $ln\dot{\overline{\epsilon}}^{in}$ against $ln\ \sigma_y$ in Figure 10b is with $n_1 = 6.51$. At the transition point between the two regimes, we have $\overline{\sigma}/K_0 = 1$, i.e., $\sigma_y = K_0$, which is estimated at 171 MPa in this case. When this is substituted in Equations (11) or (12), it becomes

$$A = \dot{\overline{\epsilon}}^{in} \tag{14}$$

at the transition point at the reference temperature, which is 3.43×10^{-6} /s in this case (Figure 10b).

The same procedure described for the 18% austenite mixture (Figure 10b) used for evaluating the transition between the two regimes was used for the two other microstructures stabilized at their previously chosen reference temperature. Table 3 presents the results. Additionally, in this table, the constant A_c in Equation (8) is estimated from the data in Table 2. The last column of the table is the coefficient of determination R^2 for the estimation of the exponent n_1.

Table 3. Drag stress at the creep–plasticity transition at the reference temperature.

Austenite Fraction f_γ	Reference Temperature T_0 (°C)	$A(T_0)$ (s^{-1})	Ac (s^{-1})	K_0 (MPa)	n_1	R^2
0	500	1.51×10^{-7}	1.95×10^{15}	332	8.50	0.896
0.18	620	3.43×10^{-6}	5.27×10^{13}	171	6.51	0.852
1.0	620	2.08×10^{-7}	3.16×10^{13}	54.0	13.6	0.814

Reference temperatures were selected to obtain sufficient experimental data points covering the two inelastic deformation regimes to provide a clear transition point and a more precise evaluation of the exponent n_1. For $f_\gamma = 0$, 500 °C is chosen as T_0, whereas for $f_\gamma = 0.18$ and 1.0, it is 620 °C.

5.3. Determination of the Young's Modulus

To complete the flow rule, it is necessary to know how the creep–plasticity transition drag stress K_0 varies with temperature, but it would require considerable experimental effort to obtain a complete curve for each temperature. There is, however, a key assumption that was posed by Engler-Pinto et al. [4] and Slavik et al. [5], which relieves us from this necessity. The assumption is stated as follows: The ratio between K_0 and the Young's modulus is considered constant at all temperatures. That is,

$$\frac{K_0(T)}{E(T)} = \kappa \tag{15}$$

$$K_0(T) = \frac{K_0(T_0)}{E(T_0)}\, E(T) = \kappa\, E(T) \tag{16}$$

where κ is a constant. This can also be formulated as follows:

It is thus important to precisely determine the Young's modulus of elasticity as a function of temperature.

This was measured in monotonic isothermal tensile tests upon fast unloading to prevent creep plasticity from introducing an error into the measurement. An Instron servo-hydraulic test facility, coupled with a Lepel induction heater and a high-temperature extensometer, was employed for this purpose.

The results are presented in Figure 11. The following polynomial best fit was determined:

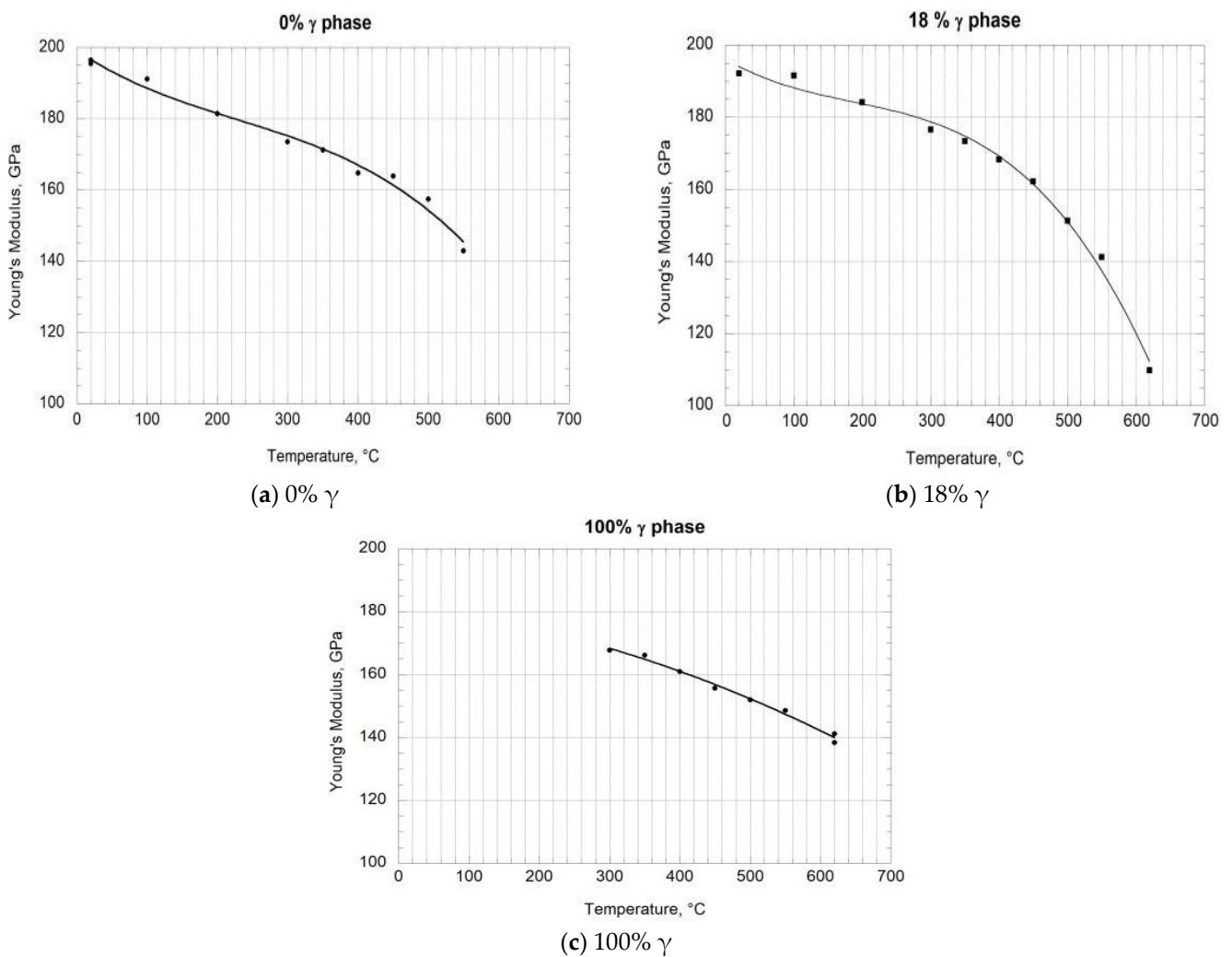$$E(T) = a_0 + a_1 T + a_2 T^2 + a_3 T^3 \tag{17}$$

(**a**) 0% γ

(**b**) 18% γ

(**c**) 100% γ

Figure 11. Young's modulus as a function of temperature.

Coefficients a_i are given in Table 4. R^2 is the coefficient of determination.

Table 4. Young's modulus Equation (16) (temperature in Celsius; modulus in GPa).

Austenite Fraction f_γ	a_0	a_1	a_2	a_3	R^2
0	199.09	−0.13106	0.00030415	-4.4241×10^{-7}	0.986
0.18	196.22	−0.11094	0.00037849	-6.7419×10^{-7}	0.992
1.0	182.01	−0.024416	-6.9947×10^{-5}	0	0.989

Using Equation (17) and data from Table 3, the constant κ in Equation (15) can be estimated. The results are given in Table 5.

Table 5. Estimation of the constant κ in Equation (16).

Austenite Fraction f_γ	Reference Temperature T_0 (°C)	K_0 (MPa)	$E(T_0)$ (GPa)	κ (MPa/GPa)
0	500	332	154.3	2.15
0.18	620	171	112.3	1.52
1.0	620	54.0	140.0	0.386

5.4. The Normalized Flow Rule

Table 2 provides data to estimate $A(T)$ in Equation (8) as a function of temperature, whereas κ in Table 5 can be employed in Equation (16) to evaluate K_0 as a function of temperature. According to Equation (7) and the scalar function expressed by Equation (9), we can thus formulate a uniaxial normalized expression for the flow rule as follows:

$$\left(\frac{\dot{\bar{\epsilon}}^{in}}{A} \right) = \left(\frac{\sigma_y}{K_0} \right)^{n_1} \quad , \quad \frac{\sigma_y}{K_0} < 1 \tag{18}$$

$$\left(\frac{\dot{\bar{\epsilon}}^{in}}{A} \right) = e^{\left[\left(\frac{\sigma_y}{K_0} \right)^{n_2} - 1 \right]}, \quad \frac{\sigma_y}{K_0} \geq 1 \tag{19}$$

The exponent n_1 related to the viscoplastic flow has been determined previously (see Table 3). The exponent n_2 is related to data in the plastic regime (those along the dashed lines in Figure 10). From Equation (19), it can be estimated as follows:

$$ln\left(\frac{\dot{\bar{\epsilon}}^{in}}{A} \right) = \left(\frac{\sigma_y}{K_0} \right)^{n_2} - 1 \tag{20}$$

Thus,

$$ln\left[ln\left(\frac{\dot{\bar{\epsilon}}^{in}}{A} \right) + 1 \right] = n_2 \, ln\left(\frac{\sigma_y}{K_0} \right) \tag{21}$$

The exponent n_2 can then be estimated from the best linear fit of $ln[ln(\dot{\epsilon}^{in}/A) + 1]$ against $ln(\sigma_y/K_0)$. The results are given in Table 6. Figure 12 illustrates the result for 18% γ.

Table 6. Estimation of the exponent n_2 from Equation (21).

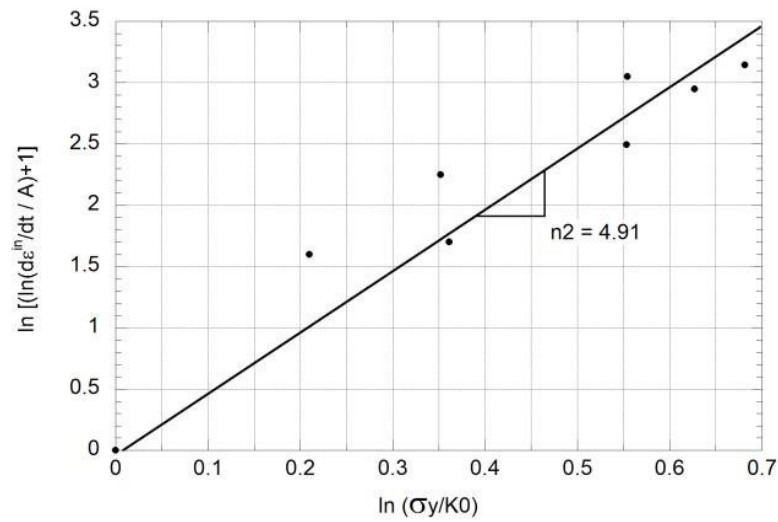| Austenite Fraction f_γ	n_2	R^2
0	7.19	0.705
0.18	4.91	0.933
1.0	22.6	0.442

Figure 12. Estimation of n_2 in the 18% γ phase.

We now have all the necessary data to formulate the flow rules according to Equations (18) and (19) and the previous tables. The results are illustrated in Figure 13.
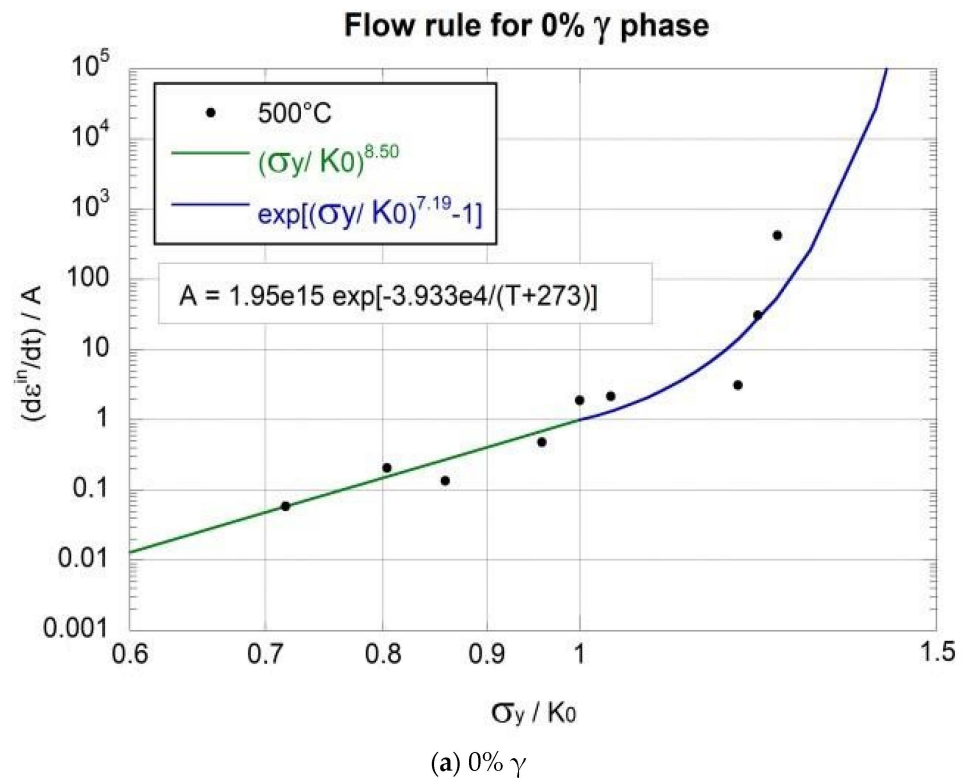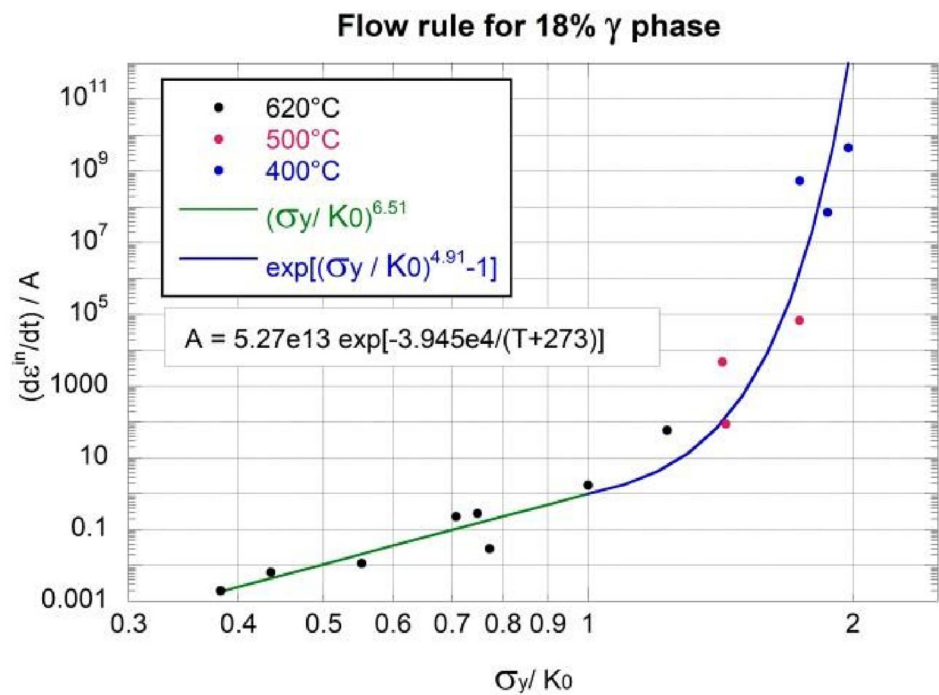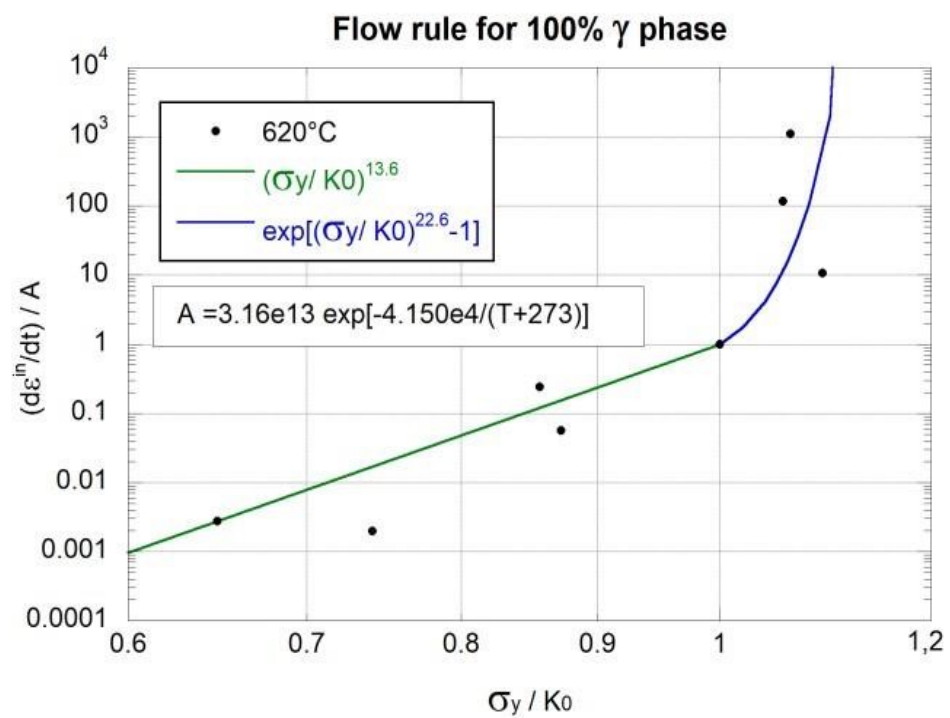

(**a**) 0% γ

Figure 13. *Cont*.

(b) 18% γ

(c) 100% γ

Figure 13. Normalized flow rules.

6. Numerical Simulation and Discussion

A constitutive relation to describe the viscoplastic behavior as a function of the equivalent stress, temperature, and state variables was developed in the previous sections. However, the determination of the parameters to characterize how the state variables, namely the drag stress and the back stress, evolve over time is not part of this study. These include the isotropic and kinematic hardening parameters as a function of the cumulative

strain and the material recovery functions at elevated temperatures. Therefore, we cannot simulate an initial level of RS since the back stress would not be zero from the start and would influence the deformation history during heating and cooling. Likewise, the drag stress will have been altered from its initial reference value.

We may, however, simulate (from Equations (18) and (19)) isothermal loadings at a constant inelastic strain rate from a virgin state and then combine the results obtained in the 100% α' and γ phases according to Equation (4) to obtain a global yield stress in an 18% γ mixture. The results are illustrated in Figure 14 for isothermal loadings at 400 °C, 500 °C, and 620 °C. On the left, the graphs illustrate independent flow rules for the three stable microstructures, whereas on the right, the 18% γ flow rule obtained from the linear rule of mixture is compared to that exclusively obtained from a constant 18% γ mixture.
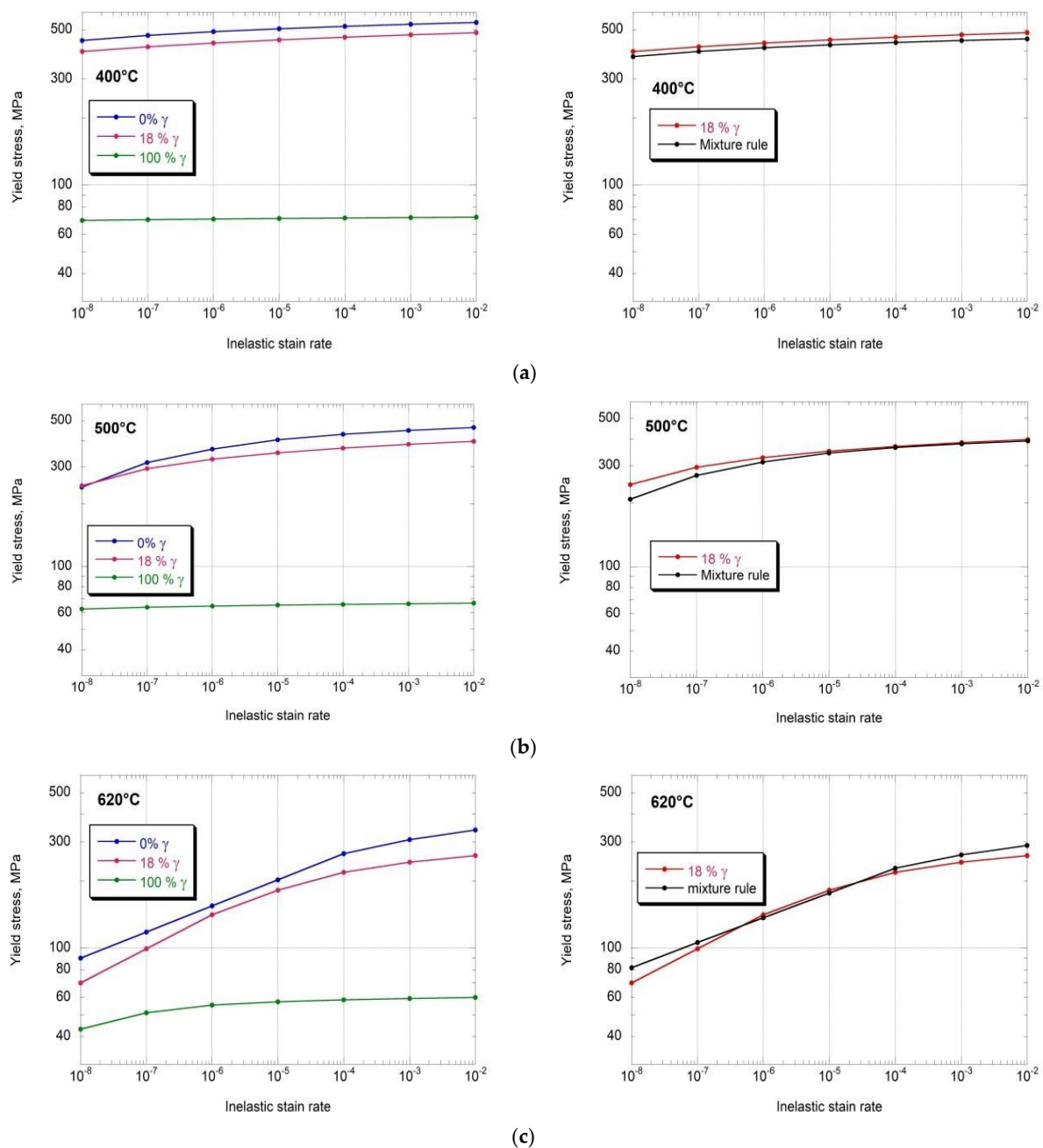

Figure 14. Numerical simulations. (**a**) Yield stress vs inelastic strain rate at 400 °C at a constant γ-phase volume fraction. (**b**) Yield stress vs inelastic strain rate at 500 °C at a constant γ-phase volume fraction. (**c**) Yield stress vs inelastic strain rate at 620 °C at a constant γ-phase volume fraction.

The phase rule seems to work well, but a mixture of only 18% γ remains insufficient to provide a very convincing demonstration since 0% γ and 18% γ mixtures have similar yield stresses. Let us mention here an important point concerning the role of austenite in martensitic steels when it comes to hardening them by surface treatment to improve their fatigue life. Austenite responds very well to this treatment. Moreover, recent work has enabled us to create, by heat treatment, a 50% γ stable mixture in nickel-enriched martensitic steel. Preliminary results on this alloy are very promising. It would therefore seem interesting to further exploit this alloy and establish the appropriate flow rule using the present approach.

It can be seen in Figure 13 that no isothermal test was carried out at 500°C in pure γ while no test was carried out in pure α′ at 620 °C (for good reason, since martensite is no longer stable at this temperature). So, for these cases, we stick only to Equations (15) and (16) to estimate the flow rule at temperatures for which no experimental tests have been or could be carried out.

In fact, no tests were carried out in all three microstructures at the same temperature. We therefore undertook to carry out three other tests (which were not used at this point to calibrate the flow rules) at 500 °C, a temperature at which the three microstructures are stable, and to compare the results to the simulation presented in Figure 14b.

These three tests are illustrated in Figure 15a–c. Inelastic strain rates are estimated at an offset of 2×10^{-4} from the yield, as discussed previously (see Figure 9). The three data points are represented by the plus signs in Figure 15d.
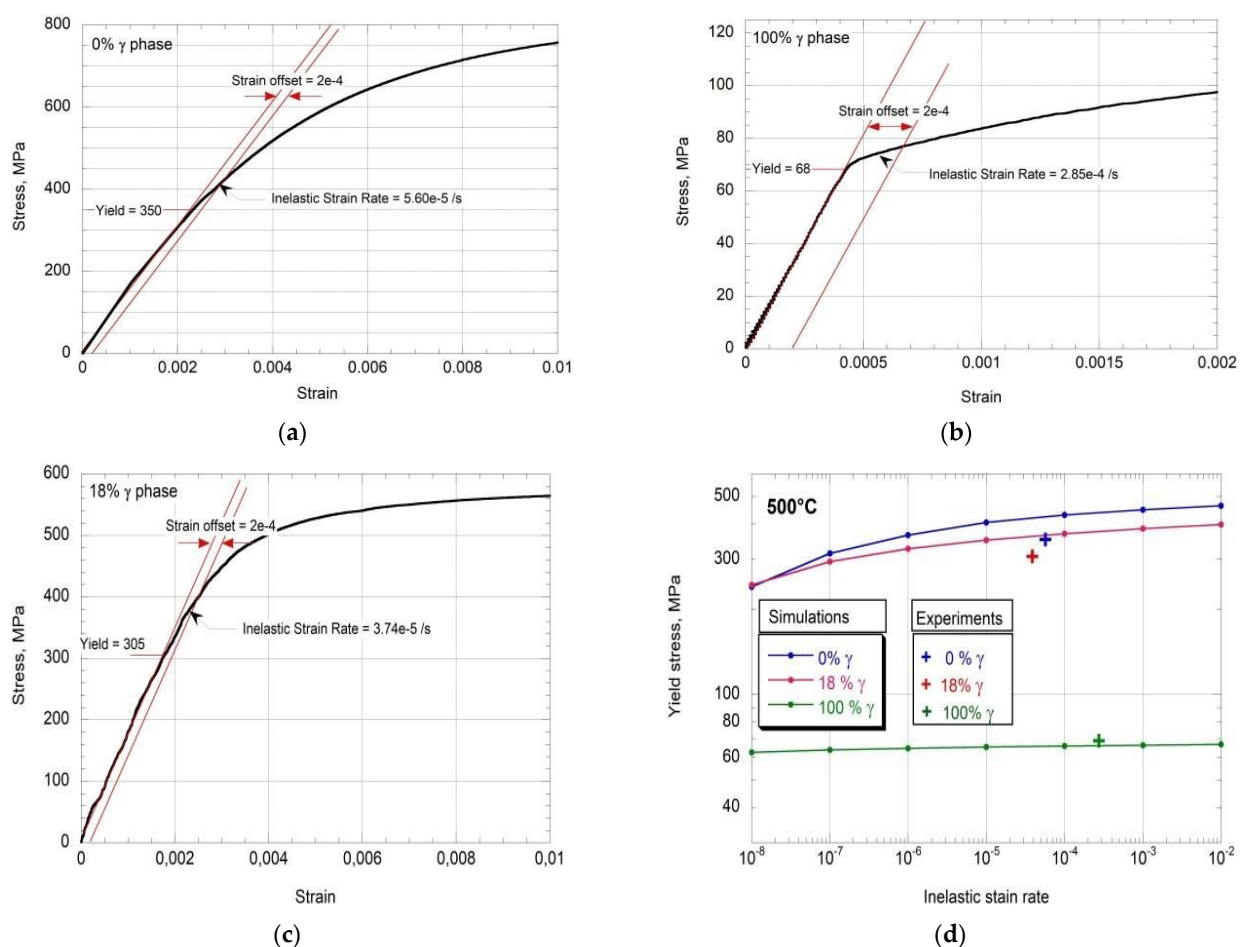

Figure 15. Experimental isothermal test results carried out at 500 °C compared to the simulations. (**a**) Isothermal test at 500 °C in pure martensite. (**b**) Isothermal test at 500 °C in pure austenite. (**c**) Isothermal test at 500 °C in a mixture with 18% γ. (**d**) Experiments compared to simulation.

The gap between simulation and experiment is higher than expected, and this can partly be explained by the assumption expressed by Equation (15). This does not compromise the unified model, but it would seem more judicious to carry out more isothermal tests at various temperatures to properly calibrate the model.

Considering the very large difference between the yield stress in the tempered martensitic state (Figure 15a) and that obtained in the tempered state with 18% austenite (Figure 15c), it is undeniable that the austenitic phase greatly conditions the plastic flow in this steel.

Another limitation that appears obvious to us is the limited number of data points used to evaluate K_o at the transition between the two deformation regimes on which the values of the exponents n_1 and n_2 depend. For example, in Figure 10b, the exponent n_1 characterizing the viscoplastic flow was determined only by tests at 620 °C, leaving only two experimental points at this temperature to evaluate the exponent n_2 characterizing the plastic flow.

There is therefore definite room for improvement. Nonetheless, we conclude that the three experimental data points obtained from the isothermal tests (Figure 15) do in fact verify the phase rule rather well. Indeed, the estimated overall yield stress from Equation (4) would be given here as $0.82 \times 350 + 0.18 \times 68$. This gives $\sigma_y^{mix} = 299$ MPa, which compares very well to the experimental value measured at 305 MPa.

7. Conclusions

In this study, a flow rule based on a unified plasticity approach has been developed. It considers the variation in the austenite content reforming during a tempering heat treatment. It would therefore be very useful for describing the viscoplastic behavior of 13Cr-4Ni steel during the PWHT manufacturing process of a turbine runner.

Considering a continuum approach, i.e., a material subject to near-uniform macroscopic stress, the rule of phase mixture should be used only at a macroscopic scale for the global distribution of the phase and not locally at the phase interface, where localized internal stresses at the nanoscale of the material are certainly developed.

The unified plasticity approach used allows an easy and straightforward implementation of the viscoplastic and plastic behavior of steel in the framework of finite element modeling of the PWHT residual stress distribution. The inelastic strain rate tensor gradually incorporates the transition from a deformation regime governed by creep mechanisms to that of plastic deformations, in which the yield stress becomes time-insensitive, typical of the behavior of steels at high strain rates. In this approach, the yield stress is the threshold stress at which the inelastic behavior of the material is observed, which in all cases is lower than the stress at the transition between creep and plastic deformation, thus defining the drag stress of the material.

The integration of microstructure-based models provided an insight into the relaxation behavior of martensitic stainless steel during heat treatment.

In conclusion, a comprehensive framework for evaluating the relaxation and redistribution of residual stresses during the PWHT has been provided. The use of unified constitutive models and their validation through isothermal constant strain rate tests afford a robust approach for future research and application in similar materials and processes.

Author Contributions: Conceptualization: J.L.; Methodology: J.L. and C.B.; Software: M.M.H., J.L. and C.B.; Validation: M.M.H. and C.B.; Formal Analysis: M.M.H. and J.L.; Investigation: M.M.H., J.L. and C.B.; Resources: J.L., M.J. and H.C.; Data Curation: J.L.; Writing—Original Draft Preparation: J.L.; Writing—Review & Editing: M.M.H., J.L., M.J. and H.C.; Visualization: J.L.; Supervision: J.L., M.J. and H.C.; Project Administration: J.L.; Funding Acquisition: J.L., M.J. and H.C. All authors have read and agreed to the published version of the manuscript.

Data Availability Statement: Raw data were generated at Institut de Recherche d'Hydro-Québec (IREQ). Derived data supporting the findings of this study are available from the corresponding author H.C. on request.

Conflicts of Interest: The authors declare no conflicts of interest.

References

1. Krempl, E. Viscoplastic models for high temperature applications. *Int. J. Solids Struct.* **2000**, *37*, 279–291. [CrossRef]
2. Li, C.; Hodgson, P.; Preuss, M.; Chen, Y.; Wu, X.; Zhu, Y.; Tian, Y.; Huang, A. Rolling-assisted direct energy deposited Inconel 718: Microstructural evolution and mechanical properties after optimized heat treatment. *J. Mater. Sci. Technol.* **2023**, *144*, 118–127. [CrossRef]
3. Lei, M.; Sun, G.; Yang, G.; Wen, B. A computational mechanical constitutive modeling method based on thermally-activated microstructural evolution and strengthening mechanisms. *Int. J. Plast.* **2024**, *173*, 103881. [CrossRef]
4. Engler-Pinto, C.C.; Sehitoglu, H.; Maier, H.J. Cyclic behavior of A1319-T7B under isothermal and non-isothermal conditions. In *Thermomechanical Fatigue Behavior of Materials: 4th Volume*; ASTM International: West Conshohocken, PA, USA, 2003.
5. Slavik, D.; Sehitoglu, H. Constitutive model for high temperature loading part I Experimental based forms of the equations. *Am. Soc. Mech. Eng. Press. Vessel. Pip. Div. (Publ.) PVP* **1987**, *123*, 65–73.
6. Sehitoglu, H. Changes in state variables at elevated temperatures. *J. Eng. Mater. Technol.* **1989**, *111*, 192–203. [CrossRef]
7. Li, Y.; Chen, H.; Du, L.; Yang, F.; Zhang, Y.; Li, D. Characterization and unified modelling of creep and viscoplasticity deformation of titanium alloy at elevated temperature. *Int. J. Plast.* **2024**, *173*, 103892. [CrossRef]
8. Hosseini, E.; Kazemi, A.; Abrinia, K.; Shahsavari, H.; Holdsworth, S.; Baghani, M. Effect of prior deformation on the subsequent creep and anelastic recovery behaviour of an advanced martensitic steel: Unified constitutive modelling. *Int. J. Mech. Sci.* **2020**, *176*, 105546. [CrossRef]
9. Fréchette, G. Étude du Comportement au Fluage de L'alliage 13Cr-4Ni en vue de Simuler la Redistribution des Contraintes Résiduelles Lors du Traitement Thermique Post-Soudage. Ph.D. Thesis, École de Technologie Supérieure, Montréal, QC, Canada, 2018.
10. Bilmes, P.; Solari, M.; Llorente, C. Characteristics and effects of austenite resulting from tempering of 13Cr–NiMo martensitic steel weld metals. *Mater. Charact.* **2001**, *46*, 285–296. [CrossRef]
11. Iwabuchi, Y.; Sawada, S. Metallurgical characteristics of a large hydraulic runner casting of type 13Cr-Ni stainless steel. In *Stainless Steel Castings*; ASTM International: West Conshohocken, PA, USA, 1982.
12. Chen, J.; Verreman, Y.; Lanteigne, J. On fracture toughness JIC testing of martensitic stainless steels. In Proceedings of the 13th International Conference on Fracture, Beijing, China, 16–21 June 2013.
13. *ASTM E975-22*; X-ray Determination of Retained Austenite in Steel with Random Crystallographic Orientation. ASTM International: West Conshohocken, PA, USA, 2023.
14. Young, R.A. The rietveld method. *Int. Union Crystallogr.* **1993**, *5*, 1–38.
15. Morawiec, M.; Grajcar, A. Some aspects of the determination of retained austenite using the Rietveld refinement. *J. Achiev. Mater. Manuf. Eng.* **2017**, *80*, 11–17. [CrossRef]
16. Song, Y.; Li, X.; Rong, L.; Li, Y. The influence of tempering temperature on the reversed austenite formation and tensile properties in Fe–13%Cr–4%Ni–Mo low carbon martensite stainless steels. *Mater. Sci. Eng. A* **2011**, *528*, 4075–4079. [CrossRef]
17. Zhang, S.; Wang, P.; Li, D.; Li, Y. Investigation of the evolution of retained austenite in Fe–13%Cr–4%Ni martensitic stainless steel during intercritical tempering. *Mater. Des.* **2015**, *84*, 385–394. [CrossRef]
18. Côté, M. Étude des Cinétiques de Transformation de Phase d'un acier Inoxydable Martensitique 13% Cr-4% Ni. Ph.D. Thesis, École de Technologie Supérieure, Montréal, QC, Canada, 2007.
19. Robichaud, P. Stabilité de L'austénite Résiduelle de L'acier Inoxydable 415 Soumis à la Fatigue Oligocyclique. Ph.D. Thesis, École de Technologie Supérieure, Montréal, QC, Canada, 2007.
20. Chaix, J. Influence de la Température de Revenu sur la Résistance du CA6NM à la Propagation des Fissures de Fatigue. Ph.D. Thesis, École Polytechnique de Montréal, Montréal, QC, Canada, 2014.
21. Leblond, J.-B.; Mottet, G.; Devaux, J. A theoretical and numerical approach to the plastic behaviour of steels during phase transformations—II. Study of classical plasticity for ideal-plastic phases. *J. Mech. Phys. Solids* **1986**, *34*, 411–432. [CrossRef]
22. Baïlon, J.P.; Dorlot, J.M. *Des Matériaux*; Presses Inter Polytechnique: Palaiseau, France, 2000.